Research Article Vol. 9, No. 7 / 1 July 2019 / Optical Materials Express 3035
Optical Materials EXPRESS

Hierarchical laser patterning of indium tin oxide thin films

NICHOLAS CHARIPAR,* RAYMOND C. Y. AUYEUNG, HEUNGSOO KIM, KRISTIN CHARIPAR, AND ALBERTO PIQUÉ

U.S. Naval Research Laboratory, 4555 Overlook Ave. SW, Washington, DC 20375, USA
**nicholas.charipar@nrl.navy.mil*

Abstract: Multiscale laser patterning of indium tin oxide thin films using the combination of direct laser interference patterning (DLIP) and laser induced periodic surface structuring (LIPSS) was studied. By balancing DLIP and LIPSS, structures in an ordered hierarchical pattern consisting of 75 nm LIPSS, 650 nm DLIP, and 50 µm laser spot size were demonstrated. The effects of laser fluence on the DLIP, LIPSS, and grain growth are discussed. The anisotropic conductance due to LIPSS was shown to exceed 50,000:1. Infrared reflectance measurements indicated that the anisotropy was uniform across the laser patterned samples.

1. Introduction

Material surfaces with micro- and nano-structured periodic patterns often exhibit enhanced functional properties compared to those of their bulk counterparts. Examples of such patterns and their applications can be found in surface engineering [1,2], metallurgy [3], optical sensors [4], metamaterials [5], and biomaterials [6]. Photolithography is one of the conventional methods used in fabricating these high-resolution patterns [7,8]; however, it involves time-consuming multi-step processes requiring complex hardware and masks designed to work on planar surfaces. An alternative method used to produce periodic patterns over extended areas operates instead by coherently combining two or more laser beams on a surface to form an interference pattern over a layer of photoresist applied to the surface. As laser technology continues to advance with ever increasing pulse energy and average power, the opportunity to apply this concept, without the photoresist layer but instead using laser interference machining, has emerged.

Laser interference machining, also referred to as direct laser interference patterning (DLIP) [9] provides a method to directly pattern materials into micron-scale or finer periodic features without intermediate processing steps associated with photolithography. Since the mid-1990's, the interference of high-intensity laser beams has been used to generate periodic patterns in semiconductors [10,11], metals [12,13], ceramics [14], and polymers [15,16]. Originally, the optical setup [10,13] of DLIP combined a minimum of two laser beams using a complex mirror system that must be aligned carefully and configured with the correct optical path lengths. More recently, a simpler optical setup with just a diffractive optical element and a biprism was demonstrated for DLIP [17].

A single laser beam (as opposed to DLIP which requires two or more beams) can also be used to create a periodic pattern of high-resolution features on a surface called Laser-induced Periodic Surface Structures (LIPSS). These structures appear in the form of ripples and have been studied extensively with laser parameters such as fluence, energy dosage, pulse duration, laser polarization and wavelength on many types of surfaces [18,19]. The periodicity of these patterns is typically on the order of the laser wavelength, denoted by low spatial frequency LIPSS (LSFL), or sub-wavelength high spatial frequency LIPSS (HSFL). The physical phenomena of the formation and growth of LIPSS are still not fully understood and under debate in the literature [20–24]. The generation of both LSFL and HSFL features from a single laser beam represents one method of hierarchical patterning [25] where the low and high frequency structures are inherently coupled.

#364843 https://doi.org/10.1364/OME.9.003035

Received 12 Apr 2019; revised 15 May 2019; accepted 29 May 2019; published 20 Jun 2019

Optical Materials EXPRESS

The combination of DLIP and LIPSS serves to decouple the spatial period of the low and high frequency structures. By including multiple interfering beams in the process, a wider range in the periodicity of patterned features can be obtained. Micron- and nano-sized periods were obtained by interfering up to 5 laser beams on a Cr/glass structure [26]. A two-beam arrangement was used in a two-step process to first produce an interference pattern and then generate a nanograting with multiple shots on bulk materials such as GaN, stainless steel, and Ti [27,28]. Recently, two interfering beams were used to write the interference pattern and generate LIPSS structures in a single step on stainless steel, polyimide, and sapphire [29]. The multi-scale periodic patterns produced by DLIP and LIPSS can result in unique surface topographies [29] which could lead to optical and electrical performance more diverse than that achieved from either DLIP or LIPSS alone. Previous research has generated these hierarchical patterns by using either a single laser beam [25], multiple laser beams or steps [26–28], or only studied the effect on bulk materials [29]. The current work reports the use of two interfering beams in a single step to create multi-scale periodic features on metal oxide films.

Transparent conductive oxides such as indium tin oxide (ITO) are well suited for multiscale patterning since they are wide bandgap semiconductors with a high electron density that simultaneously exhibit high optical transmittance and high electrical conductivity. Because of these properties, ITO is used extensively in the display industry. Sub-wavelength periodic structures have been patterned in 180 nm-thick ITO films using LIPSS with IR or visible lasers [30–32]. The morphology, optical transmission (300–2000nm), and surface resistance of these patterned ITO films were characterized in [31]; however, no anisotropy was observed in the optical or electrical measurements. At present, there have been no studies reporting the generation of simultaneous DLIP and LIPSS features in a metal oxide film.

The current study investigates the multiscale patterning of ITO films using UV ps laser pulses to produce simultaneous DLIP and LIPSS features in a single laser step. The resulting morphology was studied under different laser conditions, the polarized infrared (1–10 μm) spectrum was measured and electrical conductance characterized as a function of current orientation. The patterning of materials in a thin film structure allows for simpler characterization and analysis of its functional properties (such as electrical, optical, etc.) than those derived from its bulk counterpart.

2. Experimental

Tin-doped indium oxide (ITO) thin films were deposited on single crystal Al_2O_3 (0001) substrates by pulsed laser deposition using a KrF excimer laser (Lambda Physik LPX 300, $\lambda = 248$ nm, 30 ns pulse duration). The laser beam was rastered onto a rotating target at a pulse rate of 5 Hz and an energy density of ~ 1.5 J/cm^2. ITO films were grown in 40 mTorr of oxygen at 250°C. After deposition, the films were cooled at the same oxygen pressure. The thickness of all ITO films was determined by a stylus profilometer and averaged ~ 150 nm ± 10 nm. The electrical and optical properties of ITO films can be varied by film growth conditions, such as film growth temperature, deposition pressure or sputtering power [33,34]. The optical penetration depth of the ITO thin films at the laser processing wavelength of 355 nm was 346 nm. The sheet resistance of the 150 nm thick ITO films used in this work was determined by four-point probe measurements to be ~24 Ω/sq.

A frequency-tripled ($\lambda = 355$ nm) diode pumped solid state laser (Atlantic 355-20) provided a maximum pulse energy of 30 μJ (200 kHz) with a pulse duration of ~ 9 ps. The UV beam had a spatial TEM_{00} mode ($M^2 < 1.3$ @ 200 kHz, $\lambda = 1064$ nm) and was linearly polarized. The optical setup used for performing DLIP experiments is shown schematically in Fig. 1. An uncoated fused silica diffractive optical element (DOE) from Holo/Or (DS-231-U-N-A) divided the incoming beam into two output beams with a separation angle of 10.18°. A 1" square UV fused silica biprism (Lattice Electro Optics, Apex angle = 160°) recollimated the beams before entering

Optical Materials EXPRESS

a microscope objective (Mitutoyo M Plan Apo NUV 20X, NA = 0.4) attached to a precision Z-stage (Aerotech ANT130-110-L-ZS, 0.1 µm repeatability). The Gaussian ($1/e^2$) beam spot was measured for the 20X objective at the DLIP plane to be ~ 50 µm diameter. An optional half-wave plate was inserted before the DOE to control the polarization of the laser beam.

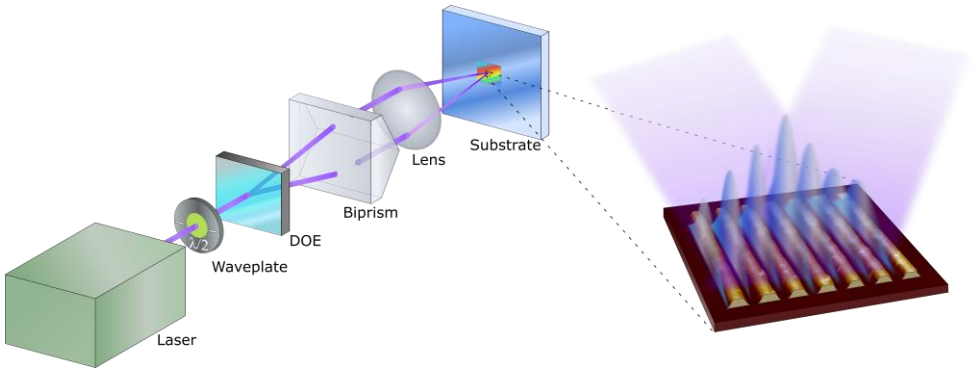

Fig. 1. Schematic of the DLIP optical setup and patterned ITO film.

The two beams exit the objective and combine at the interference plane to form fringes according to the equation:

$$\Lambda = \frac{\lambda}{2\sin(\theta/2)} \tag{1}$$

where the period or pitch, Λ, of the feature is determined by the laser wavelength λ and the angle θ between the two incident beams on the sample. The angle of incidence is determined by the separation of the two beams incident on the focusing element and its numerical aperture. Therefore, Λ can be adjusted by varying the distance between the DOE and the biprism and/or using a focusing element (lens or objective) with a different numerical aperture. For all experiments performed, the interference angle was kept constant at ~ 30° resulting in a calculated period of ~ 680 nm. Samples were secured on a vacuum chuck attached to a pair of linear air-bearing XY stages (Aerotech ABL1500, 0.2 µm repeatability). A CMOS camera collinear with the laser beam path provided a plan view of the sample through the microscope objective. Both before and after laser processing, the samples were briefly sonicated in isopropanol for ~ 30–60 s to remove any debris present on the surface. To study the evolution of the ITO microstructure, parametric experiments were performed by varying the pulse energy, scan rate, and number of pulses. An overview of the single pulse and multi-pulse processing approaches and three associated morphologies can be seen in Fig. 2.

The surface morphologies and electrical conductance of the laser patterned ITO films were characterized by atomic force microscopy (AFM) (Dimension Icon, Bruker) and anisotropic resistance measurements respectively. Additionally, polarization dependent infrared reflectance measurements were performed using an FTIR microscope (IRT-5000, Jasco) as a non-contact method to probe the anisotropic electrical properties from the infrared reflectance in cases where the patterned films were not continuous. All FTIR microscopy measurements were performed at 16X magnification (angle of incidence 27°, NA 0.57) with a spot size of 500 µm x 500 µm. The glow bar source and MCT detector were individually linearly polarized using wire grid polarizers to ensure that there was no cross-polarization error in the measurements due to scatter or surface roughness. Electrical measurements were performed using the van der Pauw method [35,36] on the ITO films.

Optical Materials EXPRESS

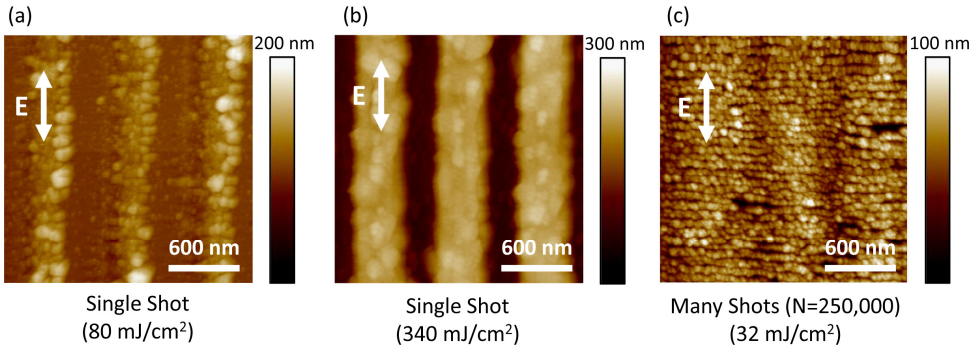

Fig. 2. AFM images of (a) single shot at 80 mJ/cm^2, (b) single shot at 340 mJ/cm^2 and (c) N = 250,000 shots at 32 mJ/cm^2. The scanned area for each image was 2 µm × 2 µm. The z-scales of (a), (b), and (c) are 200 nm, 300 nm and 100 nm, respectively. See Fig. 6 in Appendix for more details.

3. Results and discussion

The first processing approach, as shown previously in Figs. 2(a) and (b), employs a single laser pulse. Below the ablation threshold, a single laser pulse is insufficient to ablate the ITO film but raises the temperature of the ITO film significantly. This temperature increase leads to grain growth from 25 nm (as-grown ITO) (Appendix, Fig. 7) to 60 nm (below ablation threshold) by the subsequent melting and recrystallization of the ITO film. The optical absorption depth of 346 nm greatly exceeds the 150 nm thick ITO films resulting in volumetric heating throughout the thickness of the ITO thin films. In addition, there is significant heat accumulation in the ITO films as the laser period used in this work is shorter than the calculated cooling time of ~2 ms for a ~100 nm-thick ITO film and a 50 µm diameter beam spot [37]. Similar results on the laser-induced recrystallization of ITO thin films using UV and IR lasers have been previously observed [37,38]. These larger grains can enhance the electrical conductivity by reducing electron scattering at the grain boundaries. As the laser fluence is increased beyond the ablation threshold the formation of interference patterns with a period of 650 nm becomes evident as seen in Fig. 2(b).

The effect of the full range of laser fluence on the patterned ITO film morphology is shown in Fig. 3. At 90 mJ/cm^2, approximately 50 nm of the ITO film is ablated, as measured from the bottom of the AFM data to the middle of the ITO strip, where there is significant roughness at the edges of the film due to incomplete ablation and recrystallization. At 210 mJ/cm^2 the ablation depth increases to 100 nm with smoother features. At both these lower fluences, the presence of small dots could be indicative of redeposition of debris or the early stages of LIPSS formation via nanobubbles [39]. Complete ITO ablation is achieved at 340 mJ/cm^2 where the structures exhibit a further improved surface finish. Lastly, at 440 mJ/cm^2, the depth of the patterning appears to exceed the 150 nm thickness of the ITO films. This apparent depth increase is not a result of machining the substrate but rather the re-deposition of ITO on the surface of the strips. It should be noted that in the below-ablation regime, the recrystallization and grain growth occur where the laser interferes constructively (high intensity), while in the above-ablation regime the ITO film is ablated in these regions and the grain growth occurs in the low intensity regions facilitated through thermal diffusion. In the complete ablation regime (~340 mJ/cm^2) there appears to be complete melting and re-solidification of the ITO with grains of up to 100 nm. Figure 3(c) provides a summary of the ablation depth and line width as a function of fluence. It can be seen that the line width decreases with increasing fluence to a minimum of 300 nm consistent with a

Optical Materials EXPRESS

50% duty cycle (width of nanograting "ridge" divided by spatial periodicity (pitch) of features) for the measured period of 650 nm.

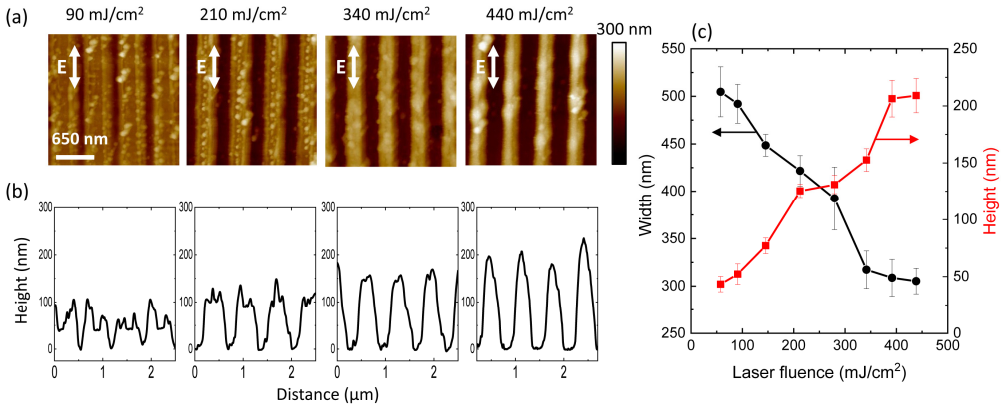

Fig. 3. (a) AFM images of single-shot DLIP patterned ITO films at 90 mJ/cm^2, 210 mJ/cm^2, 340 mJ/cm^2, and 440 mJ/cm^2. (b) Plot of the height of a cross section of the micrographs shown above. The z-scale is 300 nm for all samples. (c) Average width and height profiles of DLIP patterned ITO films as a function of laser fluence.

The second approach was based on using multiple laser shots to pattern the ITO layer as shown previously in Fig. 2(c). The multishot approach can significantly increase the temperature of the films resulting in modified material properties through re-crystallization and creation of oxygen vacancies and an altered surface topography similar to LIPSS. Oxygen vacancies have been observed previously from laser annealing of oxide films [40,41]. These modified material properties will also lead to an optical response that differs from that of the as-grown film. Examples of structures made from multiple shots are shown in Figs. 4(a), (d). The orientation of the LIPSS structure is known to be polarization dependent, therefore a half wave plate was used to rotate the polarization of the incident laser beam to align the electric field parallel and perpendicular to the DLIP interference pattern. When the electric field is aligned parallel to the interference pattern it can be seen that the LIPSS structure is orthogonal to that of the nanograting. The LIPSS period was determined by the Fourier transforms of the scanning electron micrograph in Figs. 4(a) and (d) to be 75 nm. It can be seen that the aspect ratio of the ITO grains is significantly enhanced compared to that of the single shot case where the grains did not exhibit a clear anisotropy. The LIPSS induced nanograting has a period of 75 nm and a width that is dependent on the interference pattern (650 nm) and fluence for the case where the LIPSS pattern is transverse to the DLIP structure. Conversely, the LIPSS-induced pattern parallel to the DLIP structure is not limited by the interference pattern and as such is much longer in length. The increased density of defects is most likely due to the 15% difference in fluences as well as due to the larger aspect ratio and the competition between the DLIP and LIPSS process. This is in contrast to the 2-step process of [27] where first a dual beam interference DLIP structure was formed followed by a subsequent single beam to form the LIPSS pattern. In that case, the LIPSS period was exactly three times smaller than that of the DLIP period which allowed for the DLIP pattern to serve as seeds for LIPSS formation, improving the uniformity of the LIPSS pattern. Fourier transformed SEM micrographs shown in Figs. 4(b) and (e) clearly show the 75 nm periodicity of the LIPSS and the 650 nm periodicity of the DLIP structure. The smaller periodicity of ~ 32 nm shown in Fig. 4(b) are harmonics of the 75 nm period and do not correspond to real features [42]. The multiscale or hierarchical patterning spans two orders of magnitude ranging from the 75 nm LIPSS, 650 nm DLIP, to the 50 μm laser beam diameter.

Optical Materials EXPRESS

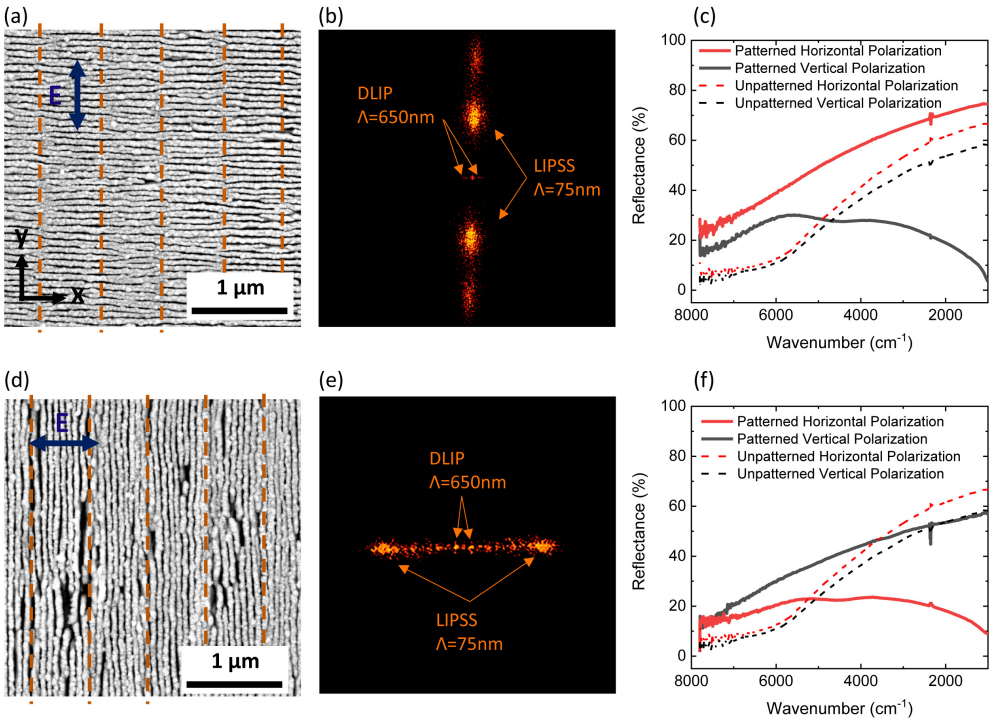

Fig. 4. (a,d) SEM images showing LIPSS structures perpendicular (32 mJ/cm^2) and parallel (37 mJ/cm^2) to DLIP. The broken lines represent the DLIP grating overlaid on the LIPSS structures. (b,e) Fourier Transform of (a,d). (c,f) Polarized infrared reflectance of horizontal and vertical LIPSS structures. Some harmonics of the 75 nm feature appear in the Fourier Transform in (b) as discussed in Ref. 42. See Fig. 8 in Appendix for more details.

To characterize the conductivity of the laser processed films, anisotropic electrical conductance measurements were performed. The resistance in the horizontal and vertical direction of the sample shown in Fig. 4(a) are Rx = 2.15 Ω and Ry = 293.50 Ω respectively. The anisotropic resistance ratio Ry/Rx is 136.5 at a laser fluence of 32 mJ/cm^2 and speed of 0.1 mm/sec. The anisotropic resistance ratio further increased to 68,660 when the fluence was increased to 39 mJ/cm^2 (not shown). In the low contrast case, the interplay between the vertical DLIP structures and horizontal LIPSS is more balanced than in the high contrast case where the LIPSS structure is dominant. This dramatic increase is due to the LIPSS spanning across the DLIP interference pattern. In the case where the DLIP and LIPSS patterns are parallel, the anisotropy is high for all cases as only a single vertical break is required to interrupt current flow. The anisotropic resistance data for Fig. 4(d) are Rx = 169.14 kΩ, Ry = 3.06 Ω, and Rx/Ry = 55,275. It should be noted that in the as-deposited ITO films, Rx = Ry = 5.2 Ω indicating that the conductivity of the patterned films is superior compared to the as-deposited films along their primary axis.

As previously mentioned, a single break in the vertical or horizontal direction is all that is required to give the appearance of high anisotropy. To address this shortfall, the infrared reflectance was measured via Fourier transform infrared spectroscopy to characterize the LIPSS induced anisotropy (Figs. 4(c) and (f)). Because the infrared reflectance was measured using a 500 µm × 500 µm spot, the resulting reflectance data is effectively the average anisotropy and clearly shows that the LIPSS is producing a continuous anisotropy rather than line defects. Horizontal and vertically polarized reflectance measurements were also performed on an

Optical Materials EXPRESS

unpatterned ITO film as a reference. The difference in reflectance between the two polarizations arises from the 30° angle of incidence as explained by the Fresnel equations. It can be seen in Figs. 4(c) and (f) that the reflectance is greatest in the direction of the LIPSS and is higher than that of the as-grown ITO film. The increase in reflectance is consistent with the increase in electrical conductance as discussed above. The sharp feature near 2360 cm^{-1} is atmospheric CO_2 as all measurements were done in atmosphere.

The evolution from an only LIPSS to a combination of a DLIP/LIPSS structure is shown in Fig. 5. At high excitation conditions the duty cycle of the pattern is inverted, the LIPSS structures form and subsequently ablate in the regions of high fluence leaving the DLIP pattern and associated microstructures.

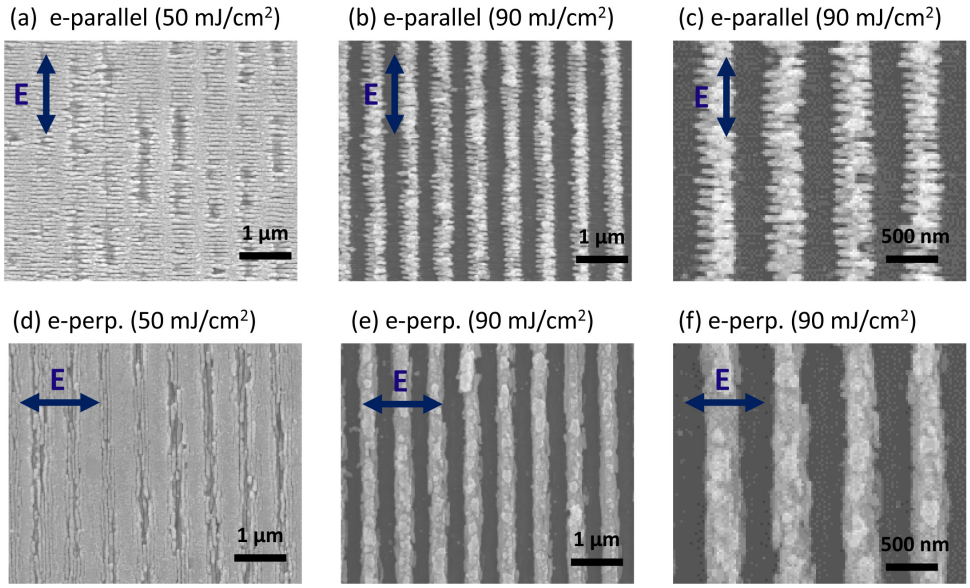

Fig. 5. SEM images showing combination of laser induced periodic surface structuring (LIPSS) and direct laser interference patterning (DLIP) in ITO films machined at 200 kHz and 5 mm/s with an electric field parallel (a-c) and perpendicular (d-f) to the nano-grating at two different laser fluences (50 and 90 mJ/cm^2). See Fig. 9 in Appendix for more details.

In the case where the electric field is aligned parallel to the DLIP pattern, distinct anisotropic ITO grains perpendicular to the vertical grating are evident. Through the careful balancing of processing parameters, a grating with a 650 nm period has been demonstrated comprised of transversely oriented anisotropic ITO grains 300 nm x 75 nm. However, in the transverse E-field case the LIPSS structure become less evident as it reinforces the DLIP pattering causing significant melting and recrystallization thereby forming a structure that is dominated by the DLIP.

4. Conclusion

Hierarchical patterning of ITO spanning more than two orders of magnitude is demonstrated via laser pattering (50 µm spot size) using simultaneous DLIP (650 nm) and LIPSS (75 nm) mechanisms. It has been shown that the dominating mechanism (DLIP vs. LIPSS) is dependent on laser processing parameters. DLIP is the dominant mechanism under high fluence conditions while LIPSS is dominant at lower fluences. The electrical anisotropy has been shown to be uniform and exceeds 50,000:1 for both parallel and transverse LIPSS structures.

Optical Materials EXPRESS

Appendix

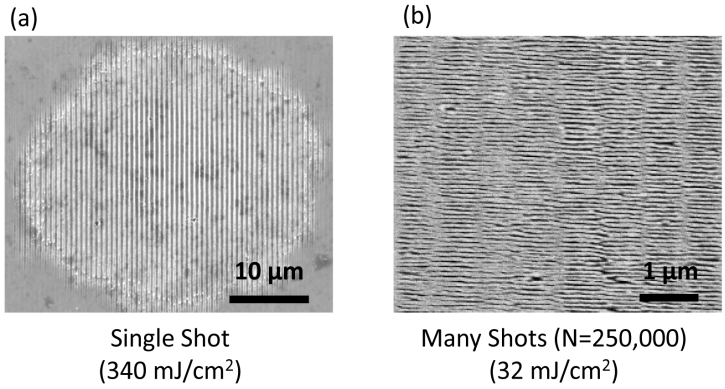

Fig. 6. SEM images of (a) a single shot with laser fluence of 340 mJ/cm^2 and (b) many laser shots (N = 250,000) with a laser fluence of 32 mJ/cm^2.

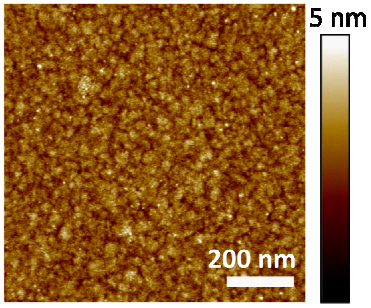

Fig. 7. AFM image (1 µm × 1 µm) of as-grown ITO film on sapphire substrate. Average grain size is ~ 25–30 nm. Note that the film surface is extremely smooth, where the z-scale is only 5 nm and the rms surface roughness is 0.45 nm.

Optical Materials EXPRESS

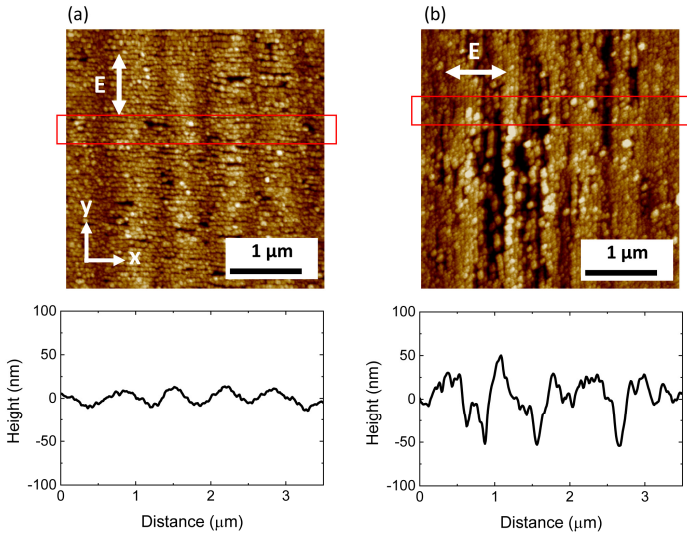

Fig. 8. AFM images (3.5 µm × 3.5 µm) with height profiles for patterned ITO films showing laser induced periodic surface structures (LIPSS) (a) perpendicular and (b) parallel to the direct laser interference patterning (DLIP). Red boxes mark the areas scanned for height profiles. (a) and (b) were obtained from similar areas in Figs. 4(a) and 4(d), respectively.

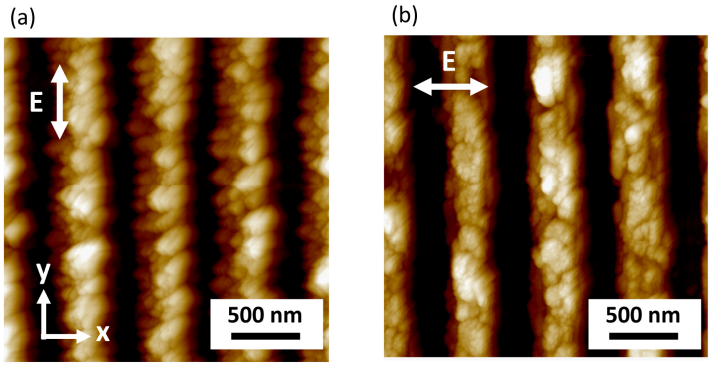

Fig. 9. AFM images (2.5 µm × 2.5 µm) showing combination of LIPSS and DLIP in ITO films laser patterned with an electric field (a) parallel and (b) perpendicular to the raster direction (y-axis) at 90 mJ/cm^2. Polarization direction is indicated in each figure. (a) and (b) were obtained from similar areas in Figs. 5(c) and 5(f), respectively.

Optical Materials EXPRESS

Funding

Office of Naval Research (ONR).

Acknowledgments

This work was funded by the Office of Naval Research (ONR) through the Naval Research Laboratory Basic Research Program.

References

1. Y. Kwon, N. Patankar, J. Choi, and J. Lee, "Design of surface hierarchy for extreme hydrophobicity," Langmuir **25**(11), 6129–6136 (2009).
2. X. Q. Dou, D. Zhang, C. L. Feng, and L. Jiang, "Bioinspired hierarchical surface structures with tunable wettability for regulating bacteria adhesion," ACS Nano **9**(11), 10664–10672 (2015).
3. A. Lasagni, C. Holzapfel, T. Weirich, and F. Mucklich, "Laser interference metallurgy: A new method for periodic surface microstructure design on multilayered metallic thin films," Appl. Surf. Sci. **253**(19), 8070–8074 (2007).
4. Z. Huang, "Microstructured silicon photodetector," Appl. Phys. Lett. **89**(3), 033506 (2006).
5. R. Kumar, A. K. Agarwal, and S. A. Ramakrishna, "Development of a metamaterial structure for large-area surfaces with specified infrared emissivity," Opt. Eng. **57**(8), 087109 (2018).
6. K. Koch, B. Bhushan, and W. Barthlott, "Multifunctional surface structures of plants: An inspiration for biomimetics," Prog. Mater. Sci. **54**(2), 137–178 (2009).
7. D. Bratton, D. Yang, J. Dai, and C. K. Ober, "Recent progress in high resolution lithography," Polym. Adv. Technol. **17**, 94–103 (2006).
8. R. P. Seisyan, "Nanolithography in microelectronics: A review," Techn. Phys. **56**(8), 1061–1073 (2011).
9. A. Aktag, S. Michalski, L. Yue, R. D. Kirby, and S.-H. Liou, "Formation of an anisotropy lattice in Co/Pt multilayers by direct laser interference patterning," J. Appl. Phys. **99**(9), 093901 (2006).
10. M. Heintze, P. V. Santos, C. E. Nebel, and M. Stutzmann, "Lateral structuring of silicon thin films by interference crystallization," Appl. Phys. Lett. **64**(23), 3148 (1994).
11. M. K. Kelly, J. Rogg, C. E. Nebel, M. Stutzmann, and S. Katai, "High-resolution thermal processing of semiconductors using pulsed-laser interference patterning," Phys. Stat. Sol. **166**, 651–657 (1998).
12. N. I. Polushkin, S. A. Gusev, and M. N. Drozdov, "Arrays of magnetic wires created in phase-separating Fe-containing alloys by interference laser irradiation," J. Appl. Phys. **81**(8), 5478–5480 (1997).
13. C. Daniel, F. Mucklich, and Z. Liu, "Periodical micro-nano-structuring of metallic surfaces by interfering laser beams," Appl. Surf. Sci. **208-209**, 317–321 (2003).
14. A. Lasagni, M. Seyler, C. Holzapfel, W. F. Maier, and F. Mucklich, "Periodical gratings in mixed-oxide films by laser-interference irradiation," Adv. Mater. **17**, 2228–2232 (2005).
15. H. M. Phillips, D. L. Callahan, and R. Sauerbrey, "Sub-100 nm lines produced by direct laser ablation in polyimide," Appl. Phys. Lett. **58**(24), 2761 (1991).
16. F. Yu, F. Mucklich, P. Li, H. Shen, S. Mathur, C.-M. Lehr, and U. Bakowsky, "In vitro cell response to a polymer surface micropatterned by laser interference lithography," Biomacromolecules **6**(3), 1160–1167 (2005).
17. M. Bieda, M. Siebold, and A. F. Lasagni, "Fabrication of sub-micron surface structures on copper, stainless steel and titanium using picosecond laser interference patterning," Appl. Surf. Sci. **387**, 175–182 (2016).
18. J. Bonse, S. Hohm, S. V. Kirner, A. Rosenfeld, and J. Kruger, "Laser-induced periodic surface structures – a scientific evergreen," IEEE J. Sel. Top. Quantum Electron. **23**(3), 9000615 (2017).
19. R. Buividas, M. Mikutis, and S. Juodkazis, "Surface and bulk structuring of materials by ripples with long and short laser pulses: Recent advances," Prog. Quantum Electron. **38**(3), 119–156 (2014).
20. S. Hohm, M. Herzlieb, A. Rosenfeld, J. Kruger, and J. Bonse, "Dynamics of the formation of laser-induced periodic surface structures (LIPSS) upon femtosecond two-color double-pulse irradiation of metals, semiconductors, and dielectrics," Appl. Surf. Sci. **374**, 331–338 (2016).
21. A. Rudenko, J.-P. Colombier, and T. E. Itina, "Nanopore-mediated ultrashort laser-induced formation and erasure of volume nanogratings in glass," Phys. Chem. Chem. Phys. **20**(8), 5887 (2018).
22. G.R.B.E. Romer, J.Z.P. Skolski, J.V. Obona, and A. J. H. in 't Veld, "Finite-difference time-domain modeling of laser-induced periodic surface structures," Phys. Procedia **56**, 1325–1333 (2014).
23. O. Varlamova, J. Reif, S. Varlamov, and M. Bestehorn, "The laser polarization as control parameter in the formation of laser-induced periodic surface structures: Comparison of numerical and experimental results," Appl. Surf. Sci. **257**(12), 5465–5469 (2011).
24. E. L. Gurevich, "Mechanisms of femtosecond LIPSS formation induced by periodic surface temperature modulation," Appl. Surf. Sci. **374**, 56–60 (2016).
25. S. Wang, L. Jiang, W. Han, J. Hu, X. Li, Q. Wang, and Y. Lu, "Hierarchical laser-induced periodic surface structures induced by femtosecond laser on the surface of a ZnO film," Appl. Phys. Expr. **11**(5), 052703 (2018).
26. Y. Nakata and N. Miyanaga, "Effect of interference pattern on femtosecond laser-induced ripple structure," Appl. Phys. A **98**(2), 401–405 (2010).

Optical Materials EXPRESS

27. K. Miyazaki and G. Miyaji, "Nanograting formation through surface plasmon fields induced by femtosecond laser pulses," J. Appl. Phys. **114**(15), 153108 (2013).
28. K. Miyazaki, G. Miyaji, and T. Inoue, "Nanograting formation on metals in air with interfering femtosecond laser pulses," Appl. Phys. Lett. **107**(7), 071103 (2015).
29. S. Alamri, F. Fraggelakis, T. Kunze, B. Krupop, G. Mincuzzi, R. Kling, and A. F. Lasagni, "On the interplay of DLIP and LIPSS upon ultra-short laser pulse irradiation," Materials **12**(7), 1018 (2019).
30. A. Pan, W. Wang, B. Liu, X. Mei, H. Yang, and W. Zhao, "Formation of high-spatial-frequency periodic surface structures on indium-tin-oxide films using picosecond laser pulses," Mater. Des. **121**, 126–135 (2017).
31. P. Liu, W. Wang, A. Pan, Y. Xiang, and D. Wang, "Periodic surface structures on the surface of indium tin oxide film obtained using picosecond laser," Opt. Laser Technol. **106**, 259–264 (2018).
32. N. Farid, P. Dasgupta, and G. M. O'Connor, "Onset and evolution of laser induced periodic surface structures on indium tin oxide thin films for clean ablation using a repetitively pulsed picosecond laser at low fluence," J. Phys. D: Appl. Phys. **51**(15), 155104 (2018).
33. H. Kim, C. M. Gilmore, A. Piqué, J. S. Horwitz, H. Mattoussi, H. Murata, Z. H. Kafafi, and D. B. Chrisey, "Electrical, optical and structural properties of indium tin oxide thin films for organic light-emitting devices," J. Appl. Phys. **86**(11), 6451 (1999).
34. Y. Wang, A. C. Overvig, S. Shrestha, R. Zhang, R. Wang, N. Yu, and L. D. Negro, "Tunability of indium tin oxide materials for mid-infrared plasmonics applications," Opt. Mater. Express **7**(8), 2727–2739 (2017).
35. L. J. van der Pauw, "A Method of measuring specific resistivity and Hall effect of discs of arbitrary shape," Philips Res. Repts **13**, 1–9 (1958).
36. O. Bierwagen, R. Pomraenke, S. Eilers, and W. T. Masselink, "Mobility and carrier density in materials with anisotropic conductivity revealed by van der Pauw measurements," Phys. Rev. B **70**(16), 165307 (2004).
37. C. W. Chien and C. W. Cheng, "Fabrication of the crystalline ITO pattern by picosecond laser with a diffractive optical element," J. Laser Micro/Nanoeng. **8**(2), 165–169 (2013).
38. T. Park and D. Kim, "Excimer laser sintering of indium tin oxide nanoparticles for fabrication thin films of variable thickness on flexible substrates," Thin Solid Films **578**, 76–82 (2015).
39. B. Huis in't Veld and H. van der Veer, "Initiation of femtosecond laser machined ripples in steel observed by scanning helium ion microscopy (SHIM)," J. Laser Micro/Nanoeng. **5**(1), 28–34 (2010).
40. H. Palneedi, J. H. Park, D. Maurya, M. Peddigari, G.-T. Hwang, V. Annapureddy, J.-W. Kim, J.-J. Choi, B.-D. Hahn, S. Priya, K. J. Lee, and J. Ryu, "Laser irradiation of metal oxide films and nanostructures: applications and advances," Adv. Mater. **30**(14), 1705148 (2018).
41. T. Szorenyi, L.D. Laude, I. Bertoti, Z. Kantor, and Zs. Geretovszky, "Excimer laser processing of indium-tin- oxide films: An optical investigation," J. Appl. Phys. **78**(10), 6211 (1995).
42. G. Miyaji and K. Miyazaki, "Fabrication of 50-nm period gratings on GaN in air through plasmonic near-field ablation induced by ultraviolet femtosecond laser pulses," Opt. Express **24**(5), 4648–4653 (2016).